Preliminary Analysis of Stress in the Newberry EGS Well NWG 55-29

Nicholas C. Davatzes[1] and Stephen H. Hickman[2]
[1]Temple University
[2]U.S. Geological Survey

Session: **Enhanced Geothermal Systems**

1. Abstract

As part of the planning for stimulation of the Newberry Volcano Enhanced Geothermal Systems (EGS) Demonstration project in Oregon, a high-resolution borehole televiewer (BHTV) log was acquired using the ALT ABI85 BHTV tool in the slightly deviated NWG 55-29 well. The image log reveals an extensive network of fractures in a conjugate set striking approximately N-S and dipping 50° that are well oriented for normal slip and are consistent with surface-breaking regional normal faults in the vicinity. Similarly, breakouts indicate a consistent minimum horizontal stress, S_{hmin}, azimuth of 092.3±17.3°. In conjunction with a suite of geophysical logs, a model of the stress magnitudes constrained by the width of breakouts at depth and a model of rock strength independently indicates a predominantly normal faulting stress regime.

Key Words: Geothermal, EGS, Image Log, Fracture, Stress, Borehole Breakout, Newberry

2. Introduction

Natural fractures play a critical role in developing an Enhanced Geothermal System (EGS) in low permeability to impermeable rock because their combination of slightly greater-than-background permeability and inherent weakness ensures interaction with the stimulation fluids or chemicals. Hydro-shearing takes advantage of these properties to invade the fracture with fluid, thereby reducing the effective normal stress and inducing small slip with the goal of producing self-propping dilation and a tortuous flow pathway (Davatzes and Hickman, 2009 and references therein). Many properties influence the slip behavior, but in this paper we focus on characterizing the natural fracture population in borehole NWG 55-29 in the west flank of Newberry Volcano, OR, and derive a model for the stresses acting on them. The analysis combines constraints from physical property logs including litho-density, neutron porosity, natural gamma, 1-arm caliper, and temperature-pressure-spinner logs and an acoustic borehole televiewer log (BHTV) acquired using the Advanced Logic Technologies (ALT) ABI85 BHTV.

3. Geologic Setting

Newberry Volcano is a shield volcano located in the Cascade Range at the intersection of three distinct structural zones: the Cascades Graben, the Brother's Fault zone, and the Basin and Range. Recently acquired LiDAR topographic data in the study area reveals N-S trending normal fault scarps in modern alluvial sediments with only minor variation in strike west of the NWG 55-29 and N-S trending alignments of fissures/vents to the east; both sets of structures indicate E-W extension in the immediate area (Cladouhos et al., 2011a). These structures reflect the geologically recent direction of the least compressive principal stress, S_{hmin}, near the Newberry EGS site. This local regional stress orientation is more uniform than might be expected for the Newberry region based on the juxtaposition of three different structural trends.

Petrographic analysis of cuttings from this borehole (Letvin, 2011) and core from the nearby GEO N-2 borehole (Fetterman and Davatzes, 2011) indicate the NWG 55-29 borehole penetrates layers of extrusive volcanic basalt, andesite, rhyolite, and related welded tuffs intruded by granodiorite and dacite below ~8610 ft MD GL (Measured Depth below Ground Level). Multi-stage stimulation is planned in the interval from the casing shoe at 6435 ft MD GL to the total depth at 10040 ft MD GL (see Cladouhos et al., 2011b).

Prior to acquisition of the image log, an inject-to-cool program was initiated to extend the depth of the logged interval to 8860 ft MD GL at a maximum temperature of 277°C. The resulting log spans the upper 2,425 ft portion of the 3,629 ft open-hole interval.

4.1 Natural Fractures

The BHTV log reveals extensive, shallowly to moderately dipping layering corresponding to volcanic flow boundaries, foliation and lithologic transitions (Figure 1). At approximately 8807 ft MD GL there is a sharp transition to massive granodiorite. These volcanic layers are cut by natural fractures with dips consistent with normal slip and similar to dips in core from the nearby GEO N-2 corehole at depths down to 4500 ft MD GL (Fetterman and Davatzes, 2011). A smaller number of natural fractures occur in the underlying granodiorite.

There are two dominant fracture sets that strike roughly N-S and dip approximately 50° to the east and west, as expected for conjugate normal fractures (Figure 2). The west-dipping set has a greater number of identified fractures, consistent with better sampling due to the slight deviation from vertical of 10.5° to 15.1° along an azimuth of 086°, as indicated by ABI85 and single shot deviation data. Poor expression of these fractures in the televiewer log suggests many of them might be at least partially healed.

The thickest, most well-developed fractures are strongly aligned with these average attitudes whereas thinner fractures have a wider distribution of attitudes. However, many of these thick fractures are characterized by either very steep or relatively shallow dips that are inconsistent with normal slip. Given that dips are determined from the boundaries of these thick fractures due to reduced image quality in the fracture interior, their true dip is less certain than for thinner fractures. Dikes have a similar attitude to natural fractures. The attitudes of primary layering such as bedding, the boundaries of volcanic flows, and foliation group into east and west dipping populations similarly to the attitude of natural fractures (Figure 2). However, their dips are generally lower: from 10 to 40°. We tentatively interpret this pattern as representing the flanks of ancient cinder cones common in the region (Cladouhos et al., 2011 and references therein). Detailed statistical analysis of the fracture population is discussed in a related manuscript by Cladouhos et al. (2011b).

4.2 Azimuth of S_{hmin} from Borehole Breakouts

Breakouts are patches of the borehole wall 180° apart that undergo compressive failure due to the elastic concentration of effective stresses around a circular borehole (Kirsch 1898; Moos and Zoback, 1990; Zoback *et al.*, 2003; Haimson, 2007). Breakouts were identified in the BHTV log as irregular patches of low amplitude and increased travel time that occur in pairs on diametrically opposed sides of the borehole (Figure 1). If the vertical stress, S_v, is taken as a principal stress (Anderson, 1951) and is approximately aligned with the borehole axis (as

assumed here) then breakouts are oriented along the minimum horizontal principal stress (S_{hmin}) azimuth (Plumb and Hickman, 1985; Moos and Zoback, 1990; Peska and Zoback, 1995; Zoback *et al.*, 2003). Following the method of Davatzes and Hickman (2010a and b), the orientation of S_{hmin} was determined from the breakouts weighted by their vertical extent in the borehole.

Clearly defined breakouts are distributed throughout the image log in the volcanic materials above 8610 ft MD GL, but are absent in the underlying granodiorite. These breakouts show a consistent azimuth independent of borehole deviation and indicate that the S_{hmin} azimuth is 092.3 ± 17.3° (Figure 3). As discussed in detail below, this azimuth of S_{hmin} in combination with the attitude of the majority of natural fractures revealed in the BHTV log is consistent with normal faulting (Figure 2).

4.3 Principal Stress Magnitudes

The stress tensor acting on the volume containing NWG 55-29 is completely characterized by the vertical principal stress and two horizontal principal stresses, all of which are counteracted by the formation fluid pressure through the effective stress principle. In this section, we model each of these four components to determine the effective stress tensor. This includes constraints on the magnitudes of horizontal principal stresses derived from the injection history, borehole deformation, and strength limits of the rock that the borehole penetrates.

4.3.1 Vertical Principal Stress and Fluid Pressure

We calculate the vertical stress (S_V) using a geophysical litho-density log spanning 1091 to 10,040 ft MD GL and an estimated average density for the overlying interval. The log data were filtered to remove spurious bulk density measurements in cases where the bulk density correction exceeds 0.2 g/cc (Asquith and Krygowski, 2004) or where the 1-arm caliper showed extensive washout. Geophysical measurements of bulk density are consistent with the bulk density estimated from the weighted average of the mineralogy measured through Rietveld Refinement of XRD of cuttings corrected for water-filled porosity using the neutron porosity log. The litho-density log data and the variation in S_v with depth calculated from these data are shown in Figure 4.

The undisturbed formation fluid pressure was derived from two equilibrated pressure logs: one on October 3, 2008, approximately 2.5 months after the borehole was completed, and a subsequent pressure log conducted September 22, 2010, prior to the inject-to-cool preparations for BHTV logging. As shown in Figure 4, the first of these logs was conducted when the borehole was open to the atmosphere, and reflects a static water table at 420 ft below GL.

4.3.2 Constraints on the Minimum Horizontal Principal Stress, S_{hmin}

In most stress analyses carried out in geothermal systems, we measure the magnitude of S_{hmin} directly using a mini hydraulic fracturing test (see Hickman and Davatzes, 2010, and references therein for details) and then constrain the magnitude of S_{Hmax} using observations of breakout width and estimates of UCS, P_f and P_m (e.g., Davatzes and Hickman, 2006). Because reliable and safe *open-hole* packers do not presently exist for use at temperatures typical of geothermal wells, these mini-frac tests are usually carried out in a short (~50 ft) and relatively impermeable section of well bore drilled just below a cemented casing shoe. Because NWG 55-29 has over 3000 ft of open hole and isolating a short section of the hole (e.g., through sanding and cement plug-back

procedures) would require a drilling rig, it is not feasible to conduct a mini-frac to determine S_{hmin} prior to stimulation due to timing and budgetary constraints. However, step-rate injection tests during the early stages of the planned EGS stimulation in NWG 55-29, with downhole pressure and temperature profile monitoring, will be used to provide direct constraints on the magnitude of S_{hmin} and depth of hydrofrac initiation, if it occurs. In addition, we will be carrying out mini-frac tests during drilling of the Newberry EGS production well during a later phase of the project, employing the procedures outlined above.

Although we currently lack a direct measurement of the magnitude of S_{hmin}, previous injection tests do constrain S_{hmin}. During the inject-to-cool operation prior to BHTV logging (Table 1), temperature-pressure logs were conducted at well head pressures (WHP) of 619 psi and 785 psi and provide complete records of pressure and temperature variation at depth (Figure 4). In another phase of the same operation, although no temperature-pressure log was obtained, maximum WHP reached 1153 psi. This WHP was achieved over three days prior to running the temperature-pressure log at 785 psi, so the downhole pressures corresponding to a WHP of 1153 psi are estimated by shifting the measured pressure profile during the 785 psi WHP survey to bring it into alignment with the maximum WHP of 1153 psi. This adjusted injecting P_f profile is plotted in Figure 4, Panels 4 and 5. In spite of the high borehole fluid pressures attained, these injection tests did not result in hydrofracture, as indicated by a lack of change in injectivity (Table 1), a lack of either pressure or temperature signatures in concurrent temperature-pressure logs (personal comm., L. Nofziger, 2011), and the lack of tensile fractures visible anywhere in the BHTV log. In addition, the apparent injectivities during this operation are similar to those measured in other un-stimulated boreholes at Newberry, including CEE 76-15 TCH, CEE 86-21 and CEE 23-22 (Spielman and Finger, 1998). Since hydrofracs form in response to borehole fluid pressure in excess of S_{hmin}, the failure to create a hydrofrac during this inject-to-cool operation provides a lower bound to the magnitude of S_{hmin}. Thus, S_{hmin} within the open-hole interval of NGW 55-29 must lie to the right of the dashed magenta line in Panels 4 and 5 of Figure 4, or else hydraulic fracturing would have occurred.

Another approach is to explore additional limits on S_{hmin} derived from a combination of an assumed tectonic environment and the frictional strength of the crust. As discussed above, it is reasonable to assume a normal faulting environment at Newberry based upon the attitude of the preponderance of natural fractures seen in the BHTV log, mapped faults at the surface, and the similarity of the S_{hmin} azimuth to the dip direction of these structures. In such a normal faulting environment, the maximum differential stress a rock can sustain is given by the difference between S_v and S_{hmin}, assuming there is a population of optimally oriented, cohesionless fractures. In accordance with the Coulomb failure criterion, frictional failure (i.e., normal faulting) would then occur at a critical magnitude of S_{hmin} given by (after Jaeger and Cook, 1979):

$$S_{hmin}^{crit} = (S_V - P_f) / [(\mu_s^2 + 1)^{1/2} + \mu_s]^2 + P_f \qquad (1)$$

where μ_s is the static coefficient of friction of preexisting faults. Mineralogy from cuttings indicates that μ_s might range from an extreme low of 0.38, consistent with the coefficient of friction of chlorite as the weakest mineral found in the cuttings (Lockner and Beeler, 2002) to 0.85, consistent with a representative rhyolite tuff from another locality (i.e., the paintbrush tuff

in the vicinity of Yucca Mountain, NV, Morrow and Byerlee, 1984). In general, however, laboratory sliding experiments on a variety of rock types show average behavior μ_s ~0.75 to 0.90 (Byerlee, 1978), but lower μ_s of 0.55 to 0.6 is also common (Jaeger and Cook, 1979; Paterson and Wong, 2005). Similar constraints on frictional strength have been derived from extensive *in situ* stress measurements in a wide range of tectonic environments (e.g., Townend and Zoback, 2000) as well as in other geothermal fields (Hickman et al., 1998, 2000; Davatzes and Hickman, 2006, 2010b; Cornet et al., 2007; Valley and Evans, 2007; Hickman and Davatzes, 2010) and support the idea that differential stress levels in the crust are generally limited by μ_s ~0.6 to 1.0. To provide frictional bounds on S_{hmin} in the vicinity of hole NWG 55-29, we use Eq. 2 to calculated S_{hmin}^{crit} corresponding to μ_s ranging from 0.55 to 0.85 (Figure 4).

4.3.3 Constraints on the Maximum Horizontal Principal Stress, S_{Hmax}

As noted earlier, breakouts span portions of the borehole wall where the compressive normal stress tangential to the borehole wall exceeds the compressive strength of the rock (see Zoback et al., 2003; Haimson, 2007). The variation of the stress components along the borehole wall is described by the 2D plane strain Kirsch equation (Kirsch, 1898). Additional sources of stress at the borehole wall include formation pore fluid pressure (P_f), the pressure difference between P_f and the fluid pressure in the borehole (P_m), and thermal stresses induced at the borehole wall by circulation of hot or cold fluids (e.g., during drilling). Following Zoback et al. (2003), the Kirsch equation is modified to include all of these contributions to the stresses causing breakout formation:

$$\sigma_{\theta\theta} = S_{Hmax} + S_{hmin} - 2(S_{Hmax} - S_{hmin})\cos(2\theta) - 2P_f - \Delta P + \sigma^{thermal} \quad (2)$$

Where $\sigma_{\theta\theta}$ is the tangential circumferential normal stress at the borehole wall, θ is the angle measured from the S_{Hmax} azimuth, and ΔP is the difference between the mud pressure and the formation fluid pressure, such that $\Delta P = P_m - P_f$. In this formulation, positive ΔP adds a component of tensile circumferential stress at the borehole wall. The term $\sigma^{thermal}$ refers to thermal circumferential stresses induced by heating or cooling the borehole wall.

Since the borehole wall is in contact with the borehole fluid and the pore pressure in rock immediately outside the borehole during breakout formation is assumed approximately equal to the borehole fluid pressure, the appropriate strength criterion for breakout formation is the uniaxial compressive strength (UCS; see discussion in Zoback et al., 2003, Zoback, 2007, and Haimson, 2007). For breakout formation, the maximum value of circumferential stress is aligned with the S_{hmin} azimuth, where θ in Eq. 2 is either 90° or 270°. Breakout width (wBO) is defined as the angle subtended by the breakout at the borehole wall and corresponds to the condition at which $\sigma_{\theta\theta} \geq$ UCS.

UCS typically varies by at least three orders of magnitude and as many as six orders of magnitude in volcanic rock (Price et al., 1993; Li and Abertson, 2003; Ma and Daemen, 2004; Entwisle et al., 2005; Frolova et al., 2005), thus large variations in breakout width can occur at constant differential stress. UCS depends strongly on the internal structure of materials, and in particular on the distribution of flaws that can locally concentrate stress and initiate failure (Lawn, 1993; Quane and Russel, 2003; Li and Albertson, 2003; Hudyma et al., 2004; Paterson and Wong, 2005). Total porosity, pore shape, and to a lesser degree, pore size impact the

magnitude of the stress concentration and thus have the strongest impact on the strength of the rock. In volcanic rocks, there can be a high degree of variability in pore size and shape due to the presence of two distinct pore populations: (1) small, sharp microcracks resulting from cooling stress, burial, and tectonic activity, and (2) potentially large, rounded vesicles that form during solidification from a melt and exsolution of volatiles.

Numerous studies have demonstrated a good empirical correlation between porosity and UCS for a variety of rock types (Ryshkewitch, 1953; Duckworth, 1953; Rzevsky and Novick,1971; Dunn et al., 1973; Price et al., 1993; Moos and Pezard, 1996; Li and Aubertin, 2003; Kleb and Vasarhelyi, 2003; Ma and Daemen, 2004; Entwisle et al., 2005; Ma et al., 2006; Zoboack, 2007). To allow for variations in UCS within the open-hole interval of NWG 55-29, we compiled UCS and porosity data (Figure 5) on relevant rock types to derive an empirical strength model by least squares fitting of an exponential function as follows:

$$UCS = 13800\exp(-0.04744\phi) \quad (3)$$

where porosity, ϕ, is in percent. In this empirical model the fitting constant in the exponential term was derived from laboratory determinations of UCS versus porosity for numerous rocks with lithologies similar to those encountered in NWG 55-29. The pre-exponential term was chosen to pass through the UCS magnitude determined from the only available complete failure envelope for welded tuff from nearby well GEO-N2 at 4281 ft MD (Ahmad Ghassemi, pers. comm, 2011). The model was then used to estimate in situ strength in NWG 55-29 from the neutron porosity log (NPHI; see Figure 4). The borehole compensated neutron porosity log measures the total porosity of the rock by direct interaction of neutrons with hydrogen atoms primarily associated with water molecules between a source and a detector, without regard to pore shape or whether the water is structured in a mineral (Hearst et al., 2000). We note here that X-ray diffraction and petrographic analysis of the cuttings in the logged interval (not presented) reveals a lack of expandable clays and only a small weight percent of zeolites in the logged interval, suggesting this log accurately represents the in situ porosity.

We explored two models for the magnitude of S_{Hmax} derived from individually measured breakout widths, the UCS at corresponding depths calculated from porosity (Eq. 3), and assuming that the magnitude of S_{hmin} was controlled by optimally oriented, critically stressed fractures with coefficients of friction of 0.55 and 0.70 (Figure 4). With these parameters, S_{Hmax} is derived from breakout width by using the conditions most favorable to their formation between when the borehole was drilled and when it was logged, which in the NWG 55-29 borehole includes: (1) minimum borehole fluid pressures given by the equilibrated fluid pressure profile (since excess borehole fluid pressure contributes tension to $\sigma_{\theta\theta}$ that inhibits breakout formation) and (2) zero stress due to cooling, in effect neglecting the thermal stress term in Eq. 2 (which would contribute a tension to $\sigma_{\theta\theta}$ that would also inhibit breakout formation). For this analysis, we filtered the more complete breakout data set to base the model solely on the average width of breakouts that occur in distinct pairs and UCS estimates based on porosity values filtered to account for adverse borehole logging conditions, such as stand-off as revealed by analysis of the 1-arm caliper log.

Under these assumptions, the majority of breakouts suggest that S_{Hmax} is less than S_V throughout the open-hole interval (Figure 4), which is consistent with geologic evidence discussed above suggesting that this site is in a predominately normal faulting stress regime. For either S_{hmin} profile (i.e., corresponding to $\mu_s = 0.55$ or 0.70), magnitudes of S_{Hmax} that exceed S_V in this model lie outside the frictional bounds on stress for normal slip and likely reflect variations in rock strength that are not accounted for in the strength model. In other words, low UCS can account for wide breakouts without invoking excessive S_{Hmax} magnitudes. We also solved Eq. 2 to define contours of S_{Hmax} as a function of UCS for a single breakout width representative of the entire population, using the statistical mode for wBO of 35.86°. In this approach the slope of the S_{Hmax} model depends on the corresponding variation in S_{hmin} and P_f, whereas the magnitude of UCS relative to a constant breakout width determines the intercept. Alternatively, the crust could be under-stressed with respect to S_{hmin}, in which case S_{hmin} would be greater than expected from Eq. 1, allowing the magnitude of S_{Hmax} to lie within the strike-slip faulting regime (i.e., $S_{Hmax} > S_v$) while still not exceeding the frictional strength of the crust.

4.3.4 Complete 3D Stress Model

The stress polygon in Figure 6 serves to summarize the analysis of stress magnitudes in the open-hole interval of NWG 55-29 by depicting combinations of horizontal principal stress magnitudes consistent with the constraints derived from borehole fluid pressure, rock strength, and breakouts (Jaeger and Cook, 1979; Moos and Zoback, 2000; Zoback, 2007). The edges of the polygon are determined from Eq. 1 for given P_f and μ_s at a depth corresponding to an interval of high fracture density at 8420 ft MD GL (Figure 2), assuming optimally oriented fractures are present in the stressed volume. Combinations of the principal stresses contained within the polygon can be supported by the frictional strength of the surrounding crust. The relative magnitudes of S_{hmin} and S_{Hmax} to S_V also determine the type of fault slip that should predominate: normal, strike slip, or reverse.

In addition, combinations of S_{hmin} and S_{Hmax} consistent with the statistical mode of the mapped breakout width for different UCS are projected into the stress polygon as a series of contours. Smaller UCS magnitudes reduce the S_{Hmax} necessary to yield this representative breakout width and allow more potential combinations of S_{hmin} and S_{Hmax} within the normal faulting stress regime (Figure 6). Since the circumferential compressive stress leading to breakout formation ($\sigma_{\theta\theta}$) *increases* rapidly with increasing S_{Hmax}, whereas increases in S_{hmin} cause a relatively small *reduction* in $\sigma_{\theta\theta}$ (Eq. 1), the slope of these contours is only at a small positive angle to the S_{hmin}/S_v axis. Thus, for a given rock strength and breakout width, relatively small increases in S_{Hmax} are required to counteract large increases in S_{hmin}. This explains the small differences in calculated S_{Hmax} magnitudes corresponding to S_{hmin} models in which $\mu_s = 0.55$ versus $\mu_s = 0.7$ (Figure 4).

From this analysis, three distinct stress states can be distinguished within the current constraints (Table 2): (1) the volume is critically stressed for normal faulting, (2) the volume is critically stressed for strike slip faulting, and (3) the volume is under stressed. In the normal faulting case, the S_{hmin} profile lies above the maximum injection pressures and in the range consistent with frictional failure at 0.6 to 0.4, below the transition to strike slip faulting. This normal faulting stress state is consistent with the most common fault attitudes mapped regionally and with fractures identified in the borehole, and consistent with breakout occurrence using the typical

range of porosity-dependent UCS. The strike slip faulting case requires high average UCS to explain the most common breakout widths and is not consistent with most mapped faults and fractures, but is otherwise similar to the normal faulting case. In the case of an under-stressed volume, the stresses are insufficient to cause slip on rocks of typical frictional strength under ambient fluid pressure conditions. This case is consistent with an over-all lack of seismicity and the absence of distinct stress rotations in the BHTV log (which would indicate localized stress rotations due to fault slip) and potentially with low permeability related to high proportions of healed (sealed) fractures. Regarding this later possibility, previous studies in a fault-hosted geothermal field at Dixie Valley, NV, showed that permeability in wells was low when individual fractures as well as the overall fault zone hosting the geothermal field were not critically stressed for friction failure (Hickman et al., 1998; Barton et al., 1998). However, the extent of this under-stressing was small, and mini-hydraulic fracturing tests still showed significant differential stresses, even in very low-permeability wells.

Most of the potential combinations of horizontal principal stresses lie within the normal faulting stress regime (Figure 6), especially when considering the probable magnitudes of UCS, which range from 6,000 to 12,000 psi in the open hole interval and average ~10,000 psi at the modeled depth (Figure 4). Although the three possible stress states listed in Table 2 are not distinguishable without additional constraint provided by a direct measurement of S_{hmin} (e.g., from a mini-hydraulic fracturing test), the under-stressed (or slightly under-stressed) NF case is probably the most likely. However, as noted above, although a lack of seismicity may be *consistent* with an under-stressed crust at this location, it is important to note that areas known to be critically stressed from extensive mini-hydraulic fracturing tests can be seismically quiescent, especially in areas of low tectonic stressing rates (e.g., Stock et al., 1985; Hickman et al, 1998). Furthermore, the great majority of sites in which *in situ* stresses have been measured directly, even in stable continental interiors, are critically stressed or near critically stressed (Townend and Zoback, 2000). Thus, the horizontal differential stresses at this site might be as large as indicated in our critically stressed NF stress model (for μ_s ~0.55), which would induce shear reactivation along well-oriented faults with only a modest increases in fluid pressure. Finally, relatively high horizontal differential stresses are consistent with the observation that breakouts in well NWG 55-29 are strongly developed and uniformly oriented (e.g., Figure 3), in spite of localized variations in rock fabric, fracturing, or dikes, which might otherwise be expected to lead to local scatter in breakout azimuths (Blake and Davatzes, 2011 and references therein).

5. Interaction of Stresses and Natural Fractures

The relative potential for slip of the natural fracture population (Figure 2) is determined by the frictional resistance of these structures, which is given by the ratio of shear to effective normal traction. This ratio is sometimes called the slip tendency, and is presented in Figure 7 assuming a stress model that is slightly under-stressed for frictional failure, as given by a magnitude for S_{hmin} in which the most highly stressed fracture has an effective slip tendency of 0.55, which means that if its μ_s is lower than 0.55 it could slip. With the current constraints on stress magnitudes, we are unable to distinguish precisely how much shear stress is available to drive slip. Nevertheless, if normal faulting predominates, this model does show: (1) slip tendency in excess of ~0.7 is not possible given constraints on the mean and differential stress (Figure 4); (2) that the same range of slip tendency occurs throughout the borehole; (3) most of the thickest fractures are under-

stressed for normal slip (and strike slip); and (4) most of the primary lithologic structures are less stressed than the natural fracture population.

The apparent stability of fractures in this interval is consistent with the overall lack of permeability in the borehole, since low rates of reactivation imply that permeability regeneration accompanying shearing of these fractures cannot keep up with the rate of mineral precipitation and healing. This interpretation is consistent with the extensive healing of fractures found in shallower core (<4500 ft) available in the GEO N-2 corehole (Fetterman and Davatzes, 2011). However, the stress model does require significant differential stress between S_V and S_{hmin} as well as between S_{hmin} and S_{Hmax}. Thus, sufficient shear stress is available to induce slip if the fluid pressure is raised (e.g., Figure 7) as part of hydraulic stimulation, whereas the overall low mean stress should facilitate dilation during slip (Jaeger and Cook, 1979; Heffer, 2002).

6. Conclusions

Analysis of the vertical stress from the litho-density log, of formation fluid pressure from the equilibrium fluid pressure logs, and of breakouts visible in the image log from NWG 55-29 suggest a predominately normal faulting stress regime, with an S_{hmin} azimuth of 092.3±17.3°. Such a stress state is consistent with the attitude of natural fractures imaged in the BHTV log and faults mapped at the surface. Fractures occur throughout the image-logged interval, including fractures well oriented for normal or oblique-normal slip in the current stress field. A strike slip stress regime is also possible, but to account for the measured distribution of breakout widths generally requires UCS much larger than currently estimated from the preliminary model of *in situ* rock strength derived from the single laboratory measurement of welded tuffs from Newberry, a review of the literature, and neutron porosity at depth. The occurrence of consistently oriented breakouts also requires a significant difference between S_{hmin} and S_{Hmax}, which suggests that fractures prone to slip will have a strong tendency to strike nearly north-south. This anisotropy would impact the shape of the volume stimulated, since previous studies in normal faulting regimes under high horizontal differential stress have shown a strong tendency for stimulation to extend in the direction of S_{Hmax}, by following the strike of highly stressed fractures (e.g., Heffer, 2002; Valley and Evans, 2007). Possible scenarios for an EGS stimulation at Newberry are numerically evaluated using the image log and other data from NWG 55-29 by Cladouhos et al. (2011a).

Detailed analysis of mineralogy from cuttings and core, temperature logs to further refine the hydrology of the borehole, and additional analyses of the stress tensor are ongoing. This work is being conducted in concert with a related, but independent study on the dilation potential and history of natural fracturing in core from Newberry borehole GEO N-2 (see Fetterman and Davatzes, 2011).

7. Acknowledgments

This study is based upon work supported by the Department of Energy under Award Number DE-EE0002777, with additional support provided by the USGS Energy Resources Program. We would like to acknowledge the support of AltaRock, Inc. for supporting this research, coordinating access to the site, and sharing borehole data, with particular thanks to Trenton Cladouhos and Laura Nofziger. Dennis King and Joseph Svitek were critical to acquisition of the image log.

8. References

Anderson, E.M., 1951. The Dynamics of Faulting and Dyke Formation (2nd Edition), Oliver & Boyd, Edinburgh.

Asquith, G. and D. Krygowski, 2004. Basic Well Log Analysis, Second Edition, AAPG Methods in Exploration Series, No. 16, The American Association of Petroleum Geoelogists, Tulsa, OK, 244 p.

Barton, C., Hickman, S., Morin, R., Zoback, M.D., and Benoit, R.,1998. Reservoir-scale fracture permeability in the Dixie Valley, Nevada, geothermal field, in *Rock Mechanics in Petroleum Engineering*, vol. 2, R. M. Holt et al. (eds.), Society of Petroleum Engineers, Richardson, TX., p. 315-322.

Blake, K., and N.C. Davatzes, 2011. Crustal Stress Heterogeneity in the Vicinity of Coso Geothermal Field, CA, *Thirty-Six Workshop on Geothermal Reservoier Engineering*, p. 11.

Byerlee, J. (1978). Friction of rocks. Pure and Applied Geophysics, v. 116, p. 615-626.

Cladouhos, T.H., S. Petty, O. Callahan, W. Osborn, S. Hickman, and N.C. Davatzes, 2011a. The role of stress modeling in stimulation planning at the Newberry Volcano EGS Demonstration Project, Proceedings, Thirty-Sixth Workshop on Geothermal Reservoir Engineering Stanford University, Stanford, California, January 31 - February 2, 2011 SGP-TR-191.

Cladouhos, T., M. Clyne, M. Nichols, S. Petty, W.L. Osborn, L. Nofziger et al., 2011b. Newbery Volcano EGS Demonstration Simulation Modeling, Geothermal Resources Council Meeting, San Diego, CA . v. 35.

Cornet, F.H., Berard, T., and Bourouis, S., 2007. How close to failure is a granite rock mass at a 5 km depth? International Journal of Rock Mechanics and Mining Sciences, v. 44, p. 47-66.

Davatzes, N.C. and S. Hickman, 2006. Stress and faulting in the Coso Geothermal Field: Update and recent results from the East Flank and Coso Wash: Proceedings, Thirty-First Workshop on Geothermal Reservoir Engineering, Stanford University, Stanford California, January 30-February 1, 2006 SGP-TR-179.

Davatzes, N.C., and S. Hickman, 2009. Fractures, stress, and fluid flow prior to stimulation of Well 27-15, Desert Peak, Nevada, EGS Project: Proceedings, Thirty-Fourth Workshop on Geothermal Reservoir Engineering Stanford University, Stanford, California, February 9-11, 2009 SGP-TR-187.

Davatzes, N., and Hickman, S., 2010a, Stress, fracture and fluid-flow analysis using acoustic and electrical image logs in hot fractured granites of the Coso Geothermal Field, California, U.S.A., in M. Pöppelreiter, Garcia-Carballido and Kraaijveld (eds.), *Dipmeter and Borehole Image Log Technology*, Amer. Assoc. Petroleum Geologists Memoir 92, Tulsa OK, pp. 259-294.

Davatzes N.C. and S. Hickman, 2010b. The feedback between stress, faulting, and fluid flows: Lessons from the Coso Geothermal Field, CA, USA [Conference] // World Geothermal Congress. - Bali, Indonesia : [s.n.], 2010.

Duckworth, W. 1953. Compression strength of porous sintered alu- mina and zirconia — 9th communication to ceramography: Dis- cussion. Journal of the American Ceramic Society, **36**(2): 68.

Dunn, D.E., L.J. LaFountain, and R.E. Jackson, 1973. Porosity dependence and mechanism of brittle fracture in sandstones. J. Geophys. Res., 78: 2403-2417.

Entwisle, D.C., P.R.N. Hobbs, L.D. Jones, D. Gunn, and M.G.Raines.2005, The relationship between effective porosity, uniaxial compressive strength and sonic velocity of intact

Borrowdale Volcanic Group core samples from Sellafield, Geotechnical and Geological Engineering, v. 23, p. 793-809.

Fetterman, J.A. and N.C. Davatzes, 2011. Fracture Generated Porosity Evolution in the Newberry Volcano Geothermal System, OR: Feedback Between Deformation and Alteration, Geothermal Resources Council National Meeting, San Diego, CA, v. 35.

Frolova, J., V. Ladygin, H. Franzson, O. Sigurðsson, V. Stefánsson, and V. Shustrov, 2005. Petrophysical Properties of Fresh to Mildly Altered Hyaloclasitie Tuffs, in *Proceedings World Geothermal Congress*, pp. 24-29, Bali, Indonesia.

Haimson, B., 2007. Micromechanisms of borehole instability leading to breakouts in rocks: International Journal of Rock Mechanics and Mining Sciences, v. 44, p. 157– 173, doi:10.1016/j.ijrmms.2006.06.002.

Hearst, J. R., P. H. Nelson, and F. L. Paillett 2000. Well logging for physical properties: A handbook for geo- physicists, geologists and engineers, 2d ed.: New York, John Wiley & Sons, 483 p.

Heffer, K., 2002. Geomechanical Influences in Water Injection Projects: An Overview, *Oil and Gas Science and Technology*, v. 57, No. 5, p. 415-422.

Hickman, S., M.D. Zoback, and R. Benoit, 1998. Tectonic controls on fault-zone permeability in a geothermal res- ervoir at Dixie Valley, Nevada, in R. M. Holt, ed., Rock mechanics in petroleum engineering: Richardson, Texas, Society of Petroleum Engineers, v. 1, p. 79–86.

Hickman, S., M.D. Zoback, C. Barton, R. Benoit, J. Svitek, and R. Summers, 2000. Stress and permeability heterogeneity within the Dixie Valley geothermal reservoir: Recent results from well 82-5, Twenty-fifth Workshop on Geothermal Reservoir Engineering Stanford University, Stanford, California, p. 256-265.

Hickman, S., and N.C. Davatzes, 2010. In-situ stress and fracture characterization for planning of an EGS stimulation in the Desert Peak geothermal field, NV: Proceedings, Thirty-fifth Workshop on Geothermal Reservoir Engineering, Stanford University, Stanford, California, February 1-3, 2010 SGP-TR-188.

Hudyma, N., B.B. Avar, M. Karakouzian, 2004. Compressive strength and failure modes of lithophysae-rich Topopah Spring Tuff specimens and analog models containing cavities, Engineering Geology, v. 73, p. 179-190.

Lawn, B., 1993. Fracture Mechanics of Brittle Solids, 2nd Edition, Cambridge University Press, Cambridge, UK, 378 p.

Jaeger, J.C., and N.G.W. Cook, 1979. Fundamentals of rock mechanics, 3d ed.: New York, Chapman and Hall, p. 28–30.

Kleb, B. and Vasarhelyi, B. (2003). Test results and empirical formulas of rock mechanical parameters of rhyolitic tuff samples from Eger's cellars, Acta Geologica Hungarica, Vol. 46, p. 301-312

Letvin, A., 2011. Analysis of Drill Cuttings Mineralogy and Geophysical Logs to Investigate Alteration History at Newberry Well 55-29 in Preparation for EGS Stimulation, [Thesis]. – RES School of Renewable Energy Science, Akureyri, Iceland. 243 p.

Li, L. and Aubertin, M. (2003). A general relationship between porosity and uniaxial strength of engineering materials, Canadian Journal of Civil Engineering, v. 30, p. 644-658.

Lockner, D. A., and N.M. Beeler, 2002. Rock failure and earthquakes, in W. K. Lee, H. Kanamori, P. Jennings, and C. Kisslinger, eds., International handbook of earth- quake and engineering seismology: San Diego, Califor- nia, Academic Press, v. 81A, p. 505–537.

Kirsch, G., 1898. Die Theorie der Elastizitat und die Bedurfnisse der Festigkeitslehre. VDI Z; 42:707. Zeitschrift des Vereines deutscher Ingenieure , 42, 797–807.

Ma, L., G. Zhao, A. Sunkara, and J.J.K. Daemen, 2006. Stress Rate Dependent Strength of a Welded Tuff in Triaxial Tests, Proceedings, 41th U.S. Rock Mechanics Symposium, Golden, Colorado, June 2006.

Ma, L. and Daemen, J.J.K., 2004. Time Dependent Mechanical Behavior of Welded Tuff, Final Technical Report, Prepared for U.S. DOE/UCCSN Cooperative Agreement DE-FC28-98NV12081. PDF available at http://hrcweb.lv-hrc.nevada.edu/qa/Report/TR-03-018-2.pdf.

Moos, D. and Pezard, A.P. (1996). Relationship between strength and physical properties of samples recovered during legs 137, 140, and 148 from hole 504B, *In:* Alt, J.C., Kinoshita, H., Stokking, L.B., and Michael, P.J. (Eds.),, *Proceedings of the Ocean Drilling Program, Scientific Results,* Vol. 148, p. 401-407.

Moos, D., and M. D. Zoback, 1990, Utilization of observations of well bore failure to constrain the orientation and magnitude of crustal stresses: Application to continental, deep sea drilling project, and ocean drilling program boreholes: Journal of Geophysical Research, v. 1000, no. B, p. 12,791–12,811.

Morrow, C. and Byerlee, J., 1984. Frictional sliding and fracture behavior of some Nevada Test Site tuffs, Proceedings of the U.S. Symposium on Rock Mechanics, 25th, p. 467-474.

Paterson, M. S., and T.-f. Wong, 2005. Experimental Rock Deformation: The Brittle Field, 346 pp., Springer, Berlin.

Peska, P., and M.D. Zoback, 1995. Compressive and tensile failure of inclined wellbores and determination of in situ stress and rock strength: Journal of Geophysical Research, v. 100, no. B7, p. 12,791–12,811.

Plumb, R., and Hickman, S., 1985, Stress-induced borehole elongation: a comparison between the four-arm dipmeter and the borehole televiewer in the Auburn Geothermal Well, *Journal of Geophysical Research*, vol. 90, p. 5513-5521.

Price, R.H., and S.J. Bauer, 1985. Analysis of the elastic and strength properties of Yucca Mountain tuff, Nevada, pp. 89 – 96, Vol. 1, Research & Engineering Applications in Rock Masses, Proceedings of the 26th U.S. Symposium on Rock Mechanics, South 19 Dakota School of Mines & Technology, June 1985, Eileen Ashworth, Editor, A.A. Balkema/Rotterdam/Boston.

Price, R.H., R.J. Martin III, and P.J. Boyd, 1993. Characteriztion of porosity in support of mechanical property analysis, SAND—92-2153C, 15 p.

Price, N.J., 1966. Fault and Joint Development in Brittle and Semi-Brittle Rock, Pergamon Press, Oxford.

Quane, S.L. and J.K. Russel, 2003. Rock strength as a metric of welding intensity in pyroclastic deposits, European Journal of Mineralogy, v. 15, p. 855-864.

Ryshkewitch, R. (1953). Compression strength of porous sintered alumina and zirconia — 9th communication to ceramography. Journal of the American Ceramic Society, **36**, 65–68.

Rzhevsky, V., and Novik, G. (1971). The physics of rocks. MIR Pub- lisher, Moscow.

Spielman, P. and Finger, J., "Well Test Results of Exploration Drilling at Newberry Crater, Oregon in 1995." Proceedings: Twenty-Third Workshop on Geothermal Reservoir Engineering, Stanford University, Jan 26-28, 1998.

Stock, J., Healy, J., Hickman, S., and Zoback, M.D., 1985. Hydraulic fracturing stress measurements at Yucca Mountain, Nevada, and relationship to the regional stress field, *Journal of Geophysical Research*, vol. 90, p. 8691-8706.

Townend, J., and M. Zoback, 2000. How faulting keeps the crust strong. Geology , 28 (5), 399-402.

Valley, B., and K.F. Evans, 2007. Stress state at Soultz-sous-Forêts to 5 km depth from wellbore failure and hydraulic observations, *Proceedings, 32nd Workshop on Geothermal Reservoir Engineering*, Stanford University, Stanford CA, SGP-TR-183.Willis-Richards, J., Watanabe, K., and Takahashi, H. (1996), Progress toward a stochastic rock mechanics model of engineered geothermal systems, *Journal Geophysical Research*, v. 101, p. 17481-17469.

Zoback, M. D., 2007. Reservoir geomechanics. Cambridge, United Kingdom, Cambridge University Press, 449 p.

Zoback, M. D., C. A. Barton, M. Brudy, D. A. Castillo, T. Finkbeiner, B. R. Grollimund, D. B. Moos, P. Peska, C. D. Ward, and D. J. Wiprut, 2003. Determination of stress orientation and magnitude in deep wells: International Journal of Rock Mechanics and Mining Sciences, v. 40, p. 1049 – 1076, doi:10.1016/j.ijrmms.2003.07.001.

Tables

Table 1: Apparent injectivity in NWG 55-29 from wellhead pressure and injection rates

Log Date	**Well-Head-Pressure (WHP)**	**Injection Rate**	**Pressure Log**	**Duration**	**Apparent Injectivity**
	[psi]	[gpm]			[gpm/psi]
2010-09-24 to 27	751	10	No	3 Days	0.013
2010-09-27	619	13	Yes		0.021
	821	17		Short-term	0.021
2010-10-11 to 20	1153	22	No	9 days	0.019
2010-10-20	785	13	Yes	Short-term (conducted during logging after 1153 psi WHP)	0.017

Table 2: Characteristics of Permissible Stress Regimes

Stress Case	Pros	Cons
Characteristics common to all stress cases	• $P_f/S_v \approx 0.34$ in the open hole • S_{hmin} profile lies above greatest injection pressure profile • Reverse faulting is incompatible with regional tectonics	• No unique constraints on horizontal principal stresses (especially S_{hmin})
NF (nearly critically stressed)	• Frictional failure occurs in the range $\mu_s = 0.4$ to 0.6 • Compatible with the majority of mapped regional faults and fractures revealed in the BHTV log • Compatible with the most common (statistical mode) wBO measurements and variable-UCS stress model • Consistent with small variation in azimuth of breakouts	• Requires relatively low static friction compared to mineralogy, Byerlee's Law or Yucca Mtn. Tuff to be currently active
SSF (nearly critically stressed)	• Frictional failure occurs in the range of $\mu_s = 0.4$ to 0.6 • Compatible with high magnitudes of S_{Hmax} predicted from some wBO measurements and variable-UCS stress model • Consistent with small variation in azimuth of breakouts	• Requires high average UCS to explain predominately low wBO if $S_{Hmax} > Sv$ • Not consistent with most faults mapped at surface or seen in BHTV log
Stable (Under-stressed)	• Consistent with lack of seismicity • Allows for expected ranges of rock $\mu_s = 0.65$-0.85, without violating lower bound on S_{hmin} imposed by inject-to-cool operations • Average UCS to explain individual wBO measurements most consistent with a NF or transitional NF-SSF stress state • NF stress state consistent with range of regional fault and borehole fracture attitudes	• None. This is the most likely stress case, although the crust could be only slightly removed from criticality (see text). • Consistent breakout azimuth requires S_{hmin} cannot approach the magnitude of S_V • Note that the mostly likely range of UCS is from 8,000 to 12,000 psi

Figure Captions

Figure 1: Unwrapped images of the travel time and amplitude signals recovered from NWG 55-29. Sinusoidal natural fractures (F) are generally subtle, the lithologic boundary (L) is indicated by an abrupt transition in amplitude, and breakouts (B) occur as patches of low amplitude (see discussion below). The three dark bands at 120° increments are from the harness that helps secure the piston assembly at the bottom of the ABI85 borehole televiewer. These images are in a magnetic north reference frame, and depth is relative to the original borehole televiewer log depths, which are 4 ft above ground level.

Figure 2: Modified tadpole plot showing the depth distribution of natural fracture and primary layering attitude from the borehole televiewer log. The azimuth of the dip direction is indicated along the x-axis and the tail of the tadpole indicates the dip relative to horizontal. Left: Natural fractures: distinguishing undifferentiated fractures, major fractures and minor fractures. Relative thickness is indicated by the symbol size. Center: Natural fracture frequency in 20 ft bins (histogram) and cumulative frequency normalized by the maximum bin frequency. Note that the colors in the center panel correspond to the categories in the left panel. Right: Layering, distinguishing bedding/banding/foliation, lithologic transitions, and dikes.

Figure 3: Statistics of breakout occurrence in borehole NWG 55-29. Left panel shows the vertical distribution of breakouts versus measured depth, where horizontal bars indicate breakout width. Red breakouts correspond to high quality picks of paired breakouts and blue breakouts are lower quality picks of single breakouts that typically occur in areas of poor image quality. Vertical yellow-filled boxes show the mean S_{hmin} azimuth ± one standard deviation, as calculated using circular statistics and weighted by the vertical extent of individual breakouts. The upper right histogram shows the distribution of breakout widths. The lower right rose diagram summarizes the cumulative height in feet of breakouts in 10° azimuthal bins.

Figure 4: Analysis of stresses versus depth for borehole NWG 55-29, *assuming a variable UCS*. From left to right: ***Panel 1:*** Fractional porosity (green) and raw bulk density (red), filtered bulk density (blue) and filtered and then smoothed bulk density (black) from the litho-density log. ***Panel 2:*** Average width of pairs of high-quality breakouts. ***Panel 3:*** UCS modeled from filtered neutron porosity (red) and UCS values used to model S_{Hmax} from breakout width (blue dots). ***Panel 4:*** Vertical stress profile with estimates of S_{Hmax} assuming S_{hmin} corresponds to the critical magnitude for normal faulting for $\mu_s = 0.55$ (shown as thin dashed line) and allowing for variable UCS as derived from panel to the left (blue dots). For comparison, the dashed black lines show S_{Hmax} for a variety of constant UCS models. The thick vertical line along the left edge of this panel indicates the extent of casing. ***Panel 5:*** Vertical stress profile assuming S_{hmin} corresponds to the critical magnitude for normal faulting at $\mu_s = 0.70$ (shown as thick dashed line) using variable UCS, as in the panel to the left. In Panels 4 and 5, the black triangles correspond to the subset of S_{Hmax} magnitudes derived from breakout width consistent the assumption of a volume critically stressed for

normal faulting. This subset is used to estimate a gradient in S_{Hmax} in the image logged interval, shown as a solid black line. Constrains on fluid pressure (P_f) are also shown in Panels 4 and 5, as identified in the key (upper right corner) and discussed in the text.

Figure 5: Compilation of published UCS data from rock types analogous to those encountered in NWG 55-29, showing various types of fits to the composite data set. The form of the correlations most commonly include power law (Rzevsky and Novick, 1971; Novik,1978; Price et al., 1993; Moos and Pezard, 1996), exponential (Ryshkewitch, 1953; Duckworth, 1953; Kleb and Vasarhelyi, 2003; Ma and Daemen, 2004; Entwisel et al., 2005; Ma et al., 2006; Zoboack, 2007), and critical porosity models derived from fracture mechanics principles (Dunn et al., 1993; Li and Aubertin, 2003). The exponential fit provided the most satisfactory representation of the composite data shown here.

Figure 6: Stress polygon showing bounds on principal stress ratios for normal faulting, strike-slip and reverse faulting stress regimes permitted by a μ_s of 0.7 (outer boundary of polygon) at a depth of 8420 ft MD GL. The best estimate of stress magnitudes at this depth is for S_{hmin}^{crit} in frictional equilibrium with μ_s =0.55 and corresponding estimates of S_{Hmax} from individual measurements of breakout width and a porosity-dependent UCS. Combinations of S_{hmin} and S_{Hmax} consistent with the statistical mode of measured breakout widths can be traced for specified magnitudes of UCS along the colored sloping lines. Three likely ranges of horizontal principal stress are shown as shaded areas: (1) normal faulting (red), (2) strike slip faulting (yellow), and (3) a system that is either normal or strike slip, but is under-stressed even for coefficient of friction, $\mu_s < 0.4$ (gray). Colored diamonds show possible stress states when S_{hmin} is at frictional equilibrium with the coefficients of friction shown, with S_{Hmax} derived from the statistical mode of wBO and using the porosity-dependent UCS appropriate to this depth (~10,000 psi; see Figure 4). Triangles indicate stress constraints obtained from breakouts, assuming S_{hmin} is in equilibrium with μ_s =0.55 and with S_{Hmax} determined using individual measurements of wBO and porosity-dependent UCS. These stress states either lie within the stress polygons for normal or strike-slip faulting (as indicated) or exceed the frictional strength of the crust in a strike-slip faulting stress regime (non-physical case).

Figure 7: Slip tendency determined by the ratio of shear to effective normal stress acting on natural fractures (left) and primary layering (right) versus depth, assuming that S_{hmin} is in frictional equilibrium with a μ_s of 0.55. These calculations are based on a constant gradient in P_p, S_{hmin}, S_v, and S_{Hmax} over the image-logged interval of NWG 55-29, as shown in Figure 4, Panel 4. These profiles of principal stresses and fluid pressure are not forced through the origin and thus honor the stress magnitude model.

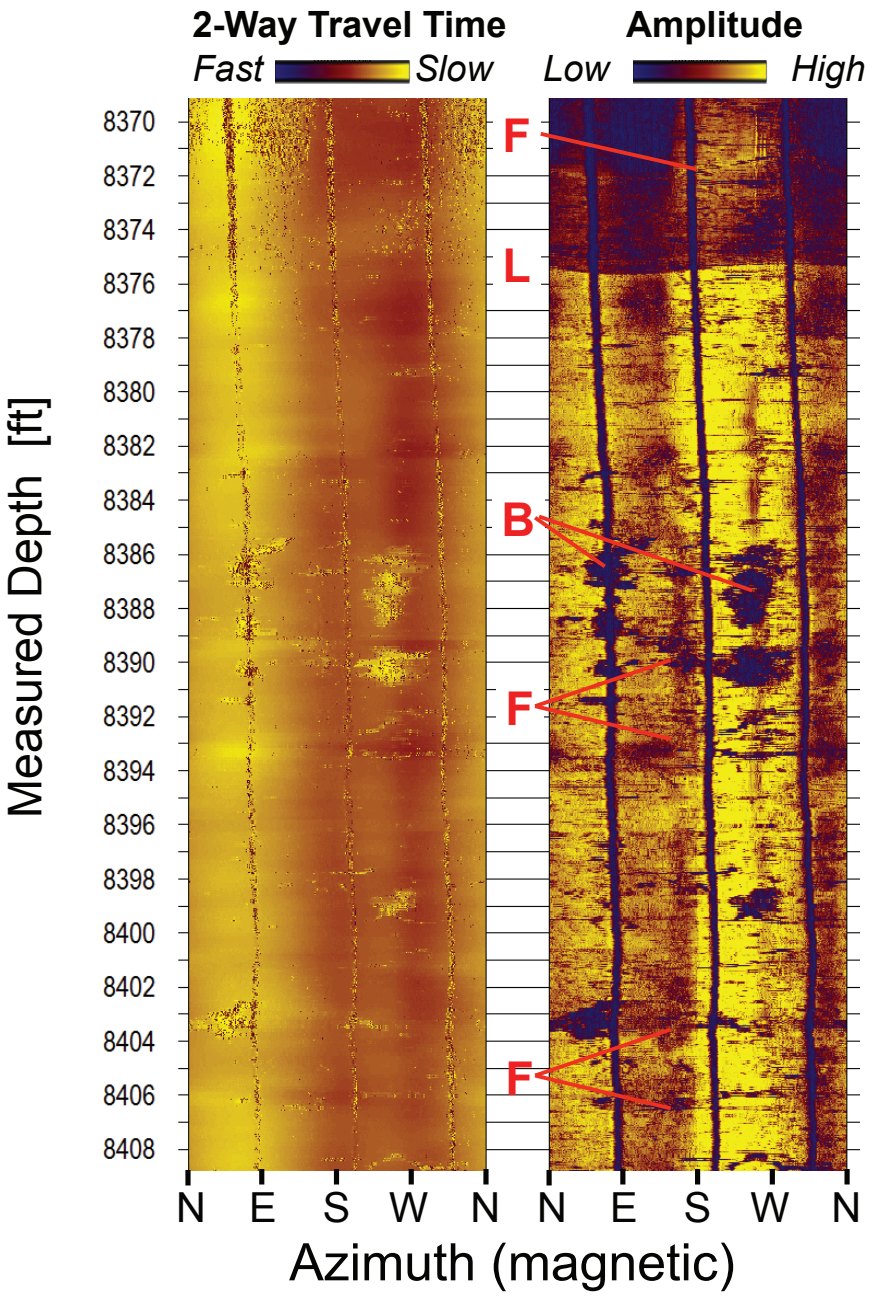
2-Way Travel Time
Fast
Slow
Amplitude
Low
High
Measured Depth [ft]
8370
8372
8374
8376
8378
8380
8382
8384
8386
8388
8390
8392
8394
8396
8398
8400
8402
8404
8406
8408
F
L
B
F
F
N E S W N N E S W N
Azimuth (magnetic)

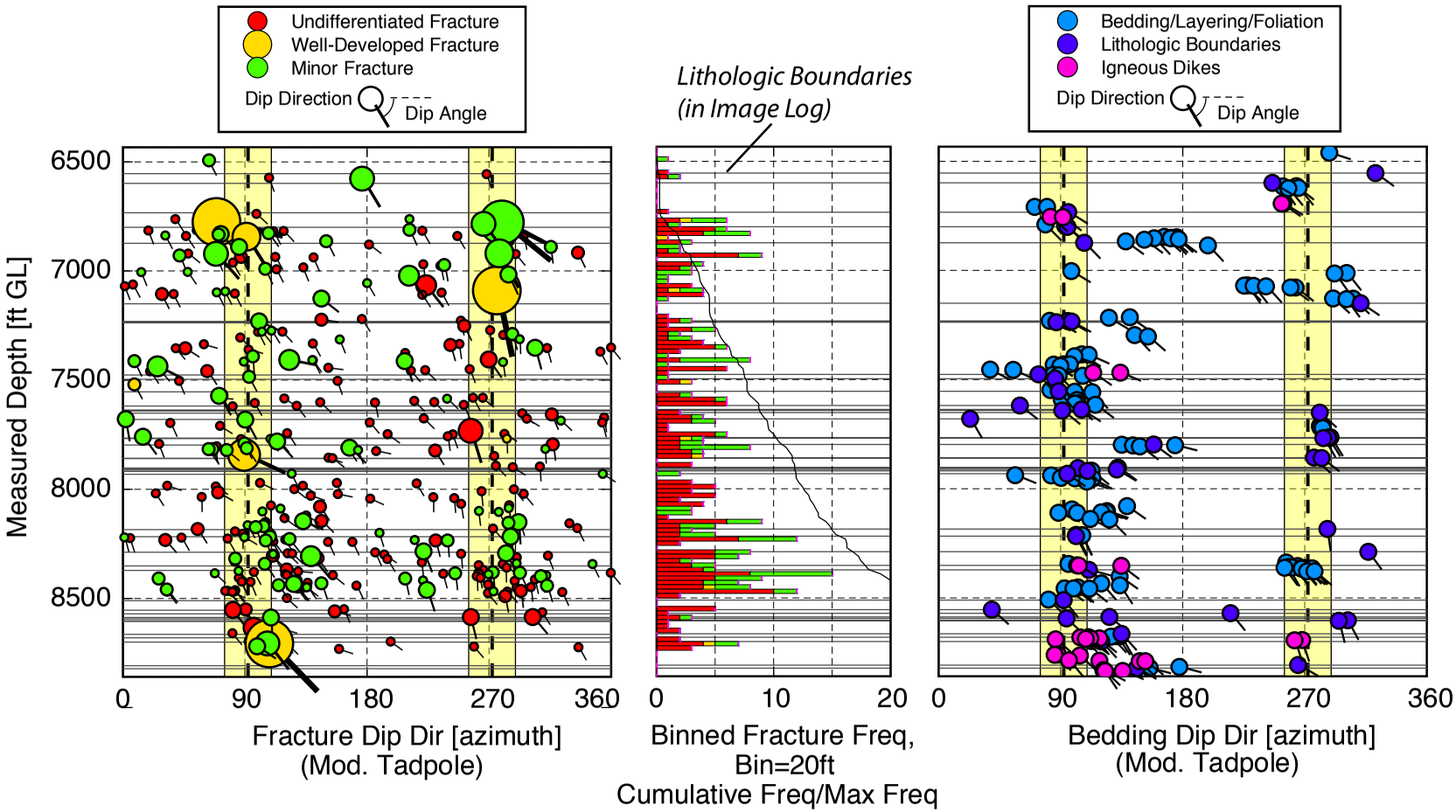
Undifferentiated Fracture
Well-Developed Fracture
Minor Fracture
Dip Direction
Dip Angle
Lithologic Boundaries
(in Image Log)
Bedding/Layering/Foliation
Lithologic Boundaries
Igneous Dikes
Dip Direction
Dip Angle
Measured Depth [ft GL]
6500
7000
7500
8000
8500
0
90
180
270
360
Fracture Dip Dir [azimuth]
(Mod. Tadpole)
0
10
20
Binned Fracture Freq,
Bin=20ft
Cumulative Freq/Max Freq
0
90
180
270
360
Bedding Dip Dir [azimuth]
(Mod. Tadpole)

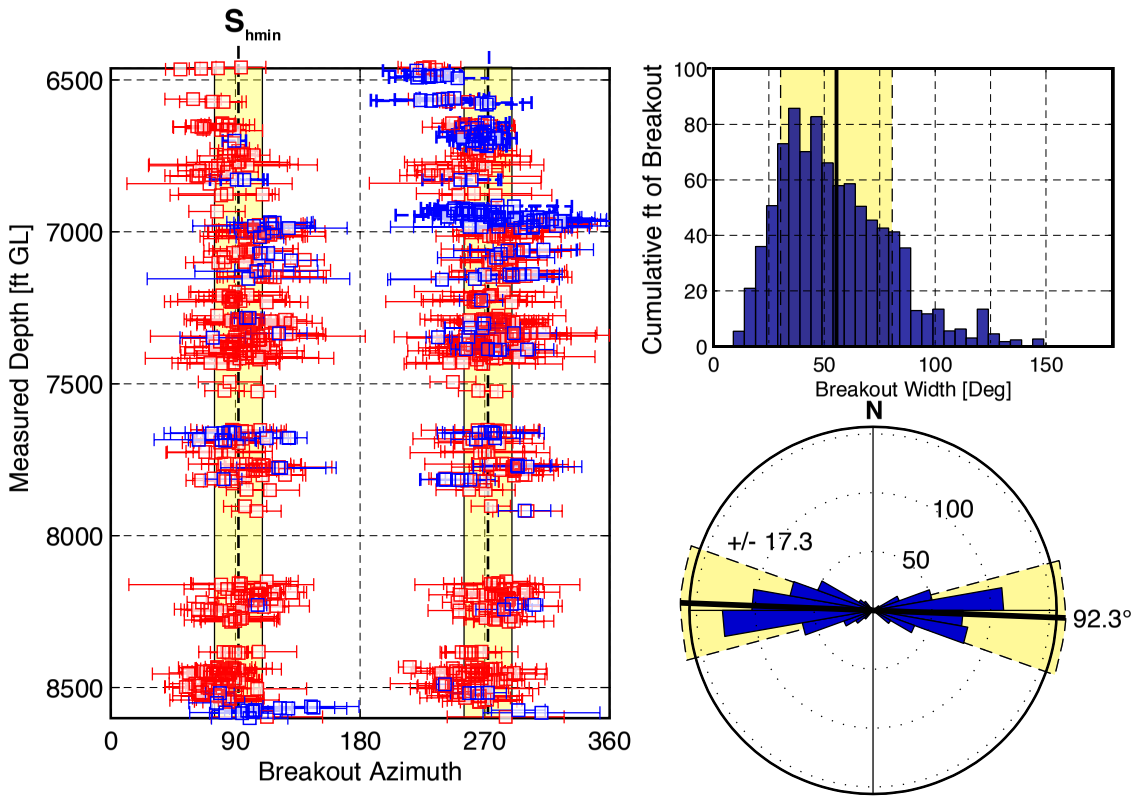
S hmin
Measured Depth [ft GL]
6500
7000
7500
8000
8500
0
90
180
270
360
Breakout Azimuth
Cumulative ft of Breakout
100
80
60
40
20
0
0
50
100
150
Breakout Width [Deg]
N
100
50
+/- 17.3
92.3°

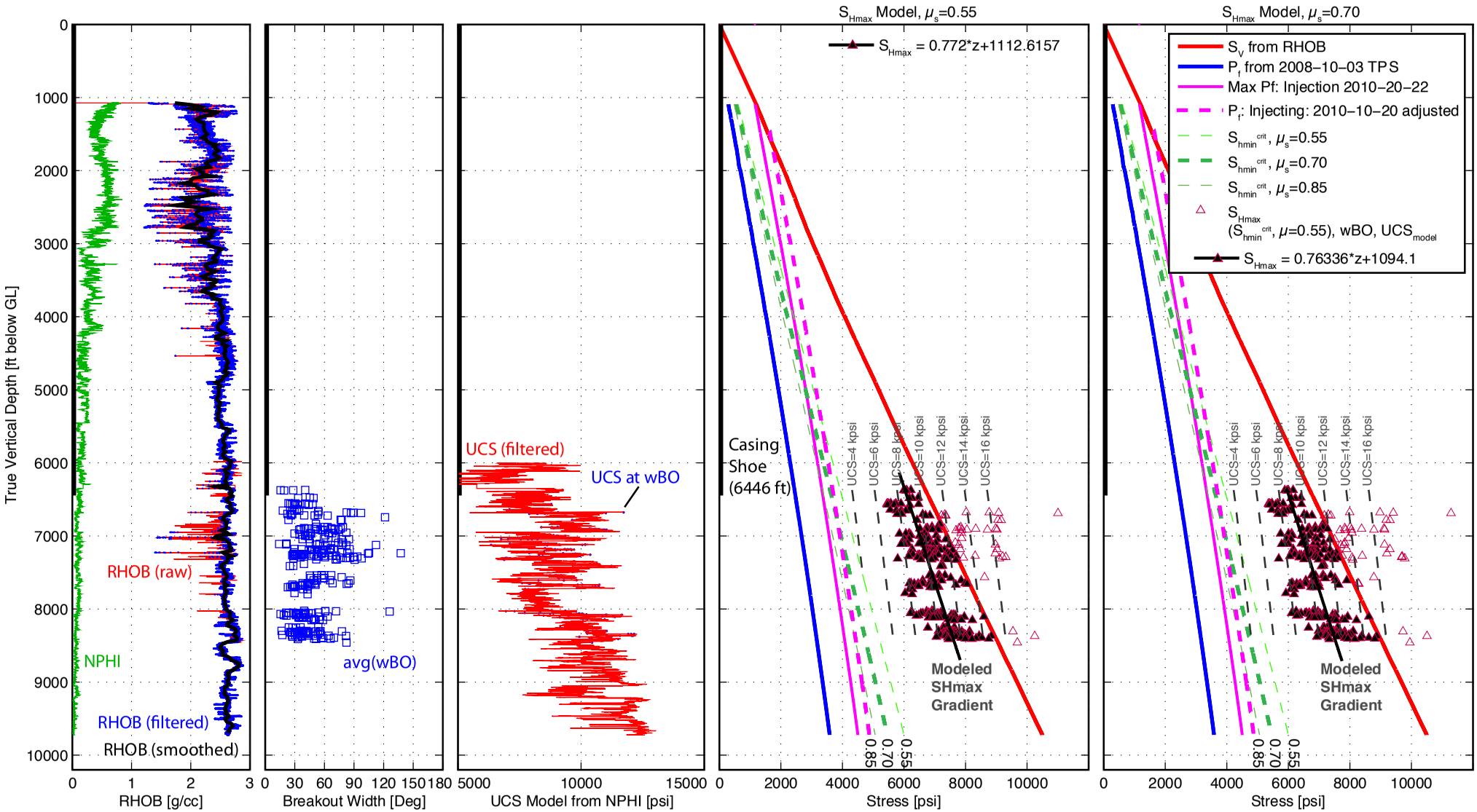
True Vertical Depth [ft below GL]
RHOB [g/cc]
RHOB (raw)
NPHI
RHOB (filtered)
RHOB (smoothed)
Breakout Width [Deg]
avg(wBO)
UCS Model from NPHI [psi]
UCS (filtered)
UCS at wBO
S_Hmax Model, μs=0.55
S_Hmax = 0.772*z+1112.6157
Casing Shoe (6446 ft)
UCS=4 kpsi
UCS=6 kpsi
UCS=8 kpsi
UCS=10 kpsi
UCS=12 kpsi
UCS=14 kpsi
UCS=16 kpsi
Modeled SHmax Gradient
0.85
0.70
0.55
Stress [psi]
S_Hmax Model, μs=0.70
S_V from RHOB
P_f from 2008–10–03 TPS
Max Pf: Injection 2010–20–22
P_f: Injecting: 2010–10–20 adjusted
S_hmin^crit, μs=0.55
S_hmin^crit, μs=0.70
S_hmin^crit, μs=0.85
S_Hmax (S_hmin^crit, μ=0.55), wBO, UCS_model
S_Hmax = 0.76336*z+1094.1

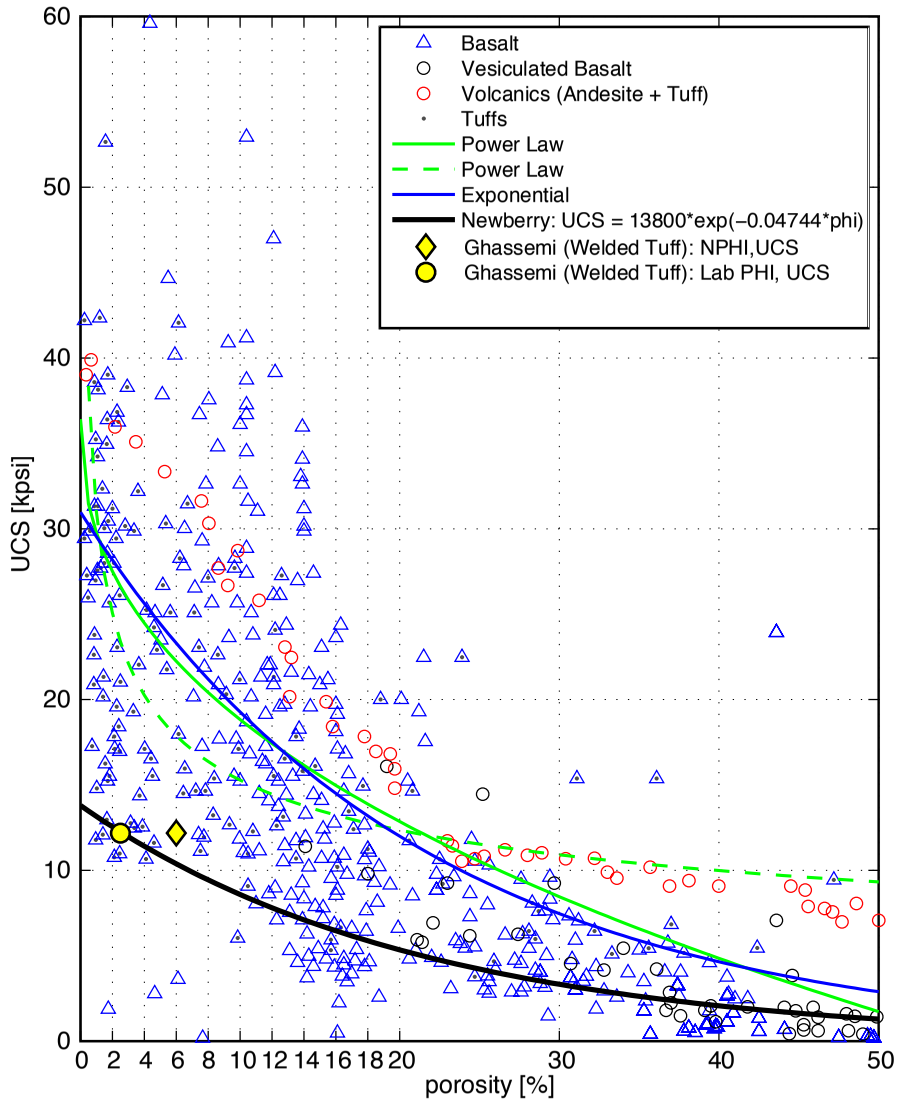
Basalt
Vesiculated Basalt
Volcanics (Andesite + Tuff)
Tuffs
Power Law
Power Law
Exponential
Newberry: UCS = 13800*exp(−0.04744*phi)
Ghassemi (Welded Tuff): NPHI,UCS
Ghassemi (Welded Tuff): Lab PHI, UCS
UCS [kpsi]
porosity [%]
0
10
20
30
40
50
60
0 2 4 6 8 10 12 14 16 18 20 30 40 50

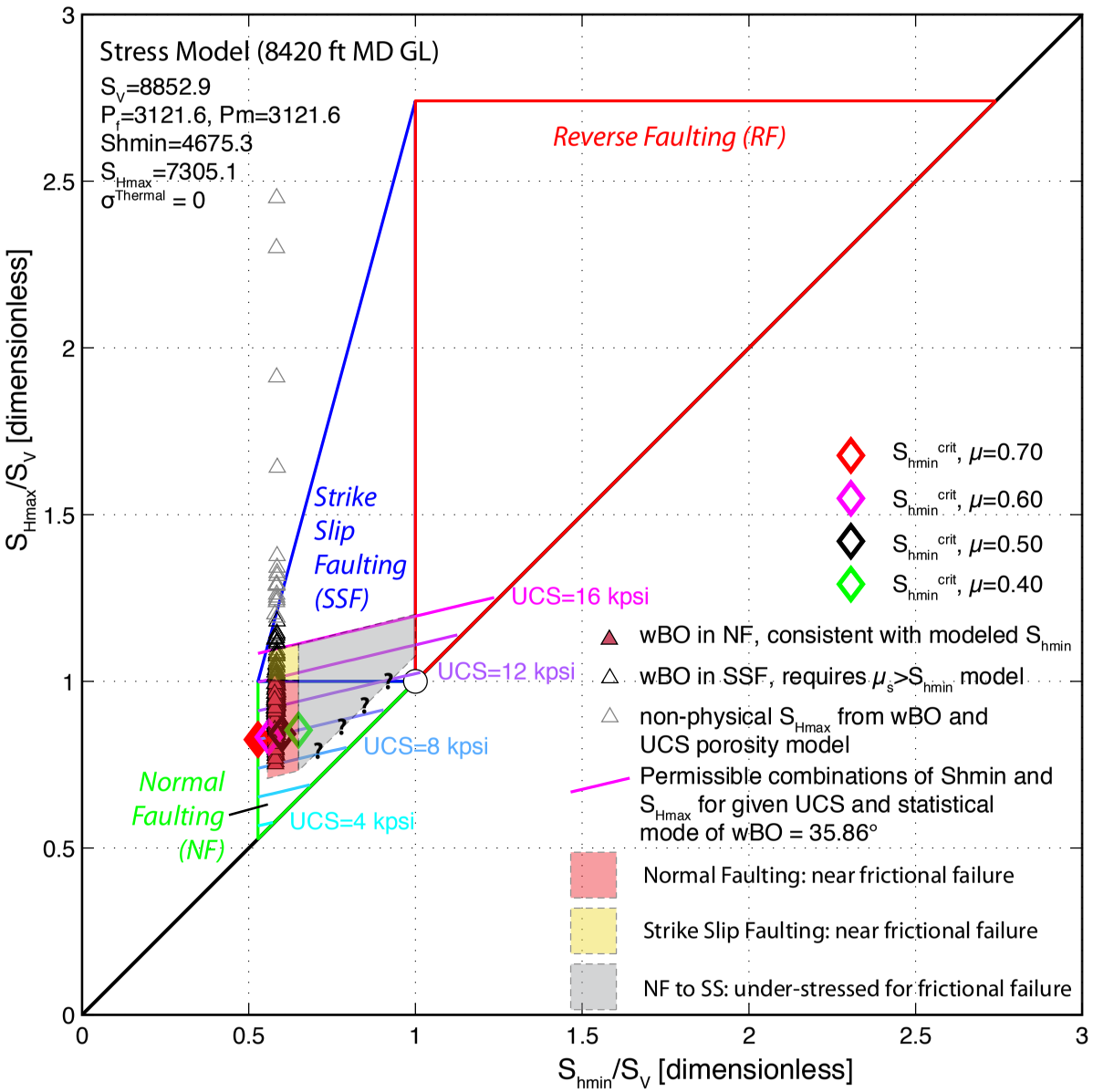
Stress Model (8420 ft MD GL)
S_V=8852.9
P_f=3121.6, Pm=3121.6
Shmin=4675.3
S_{Hmax}=7305.1
$\sigma^{Thermal}$ = 0
Reverse Faulting (RF)
Strike Slip Faulting (SSF)
Normal Faulting (NF)
UCS=16 kpsi
UCS=12 kpsi
UCS=8 kpsi
UCS=4 kpsi
S_{hmin}^{crit}, μ=0.70
S_{hmin}^{crit}, μ=0.60
S_{hmin}^{crit}, μ=0.50
S_{hmin}^{crit}, μ=0.40
wBO in NF, consistent with modeled S_{hmin}
wBO in SSF, requires μ_s>S_{hmin} model
non-physical S_{Hmax} from wBO and UCS porosity model
Permissible combinations of Shmin and S_{Hmax} for given UCS and statistical mode of wBO = 35.86°
Normal Faulting: near frictional failure
Strike Slip Faulting: near frictional failure
NF to SS: under-stressed for frictional failure
S_{Hmax}/S_V [dimensionless]
S_{hmin}/S_V [dimensionless]
0
0.5
1
1.5
2
2.5
3

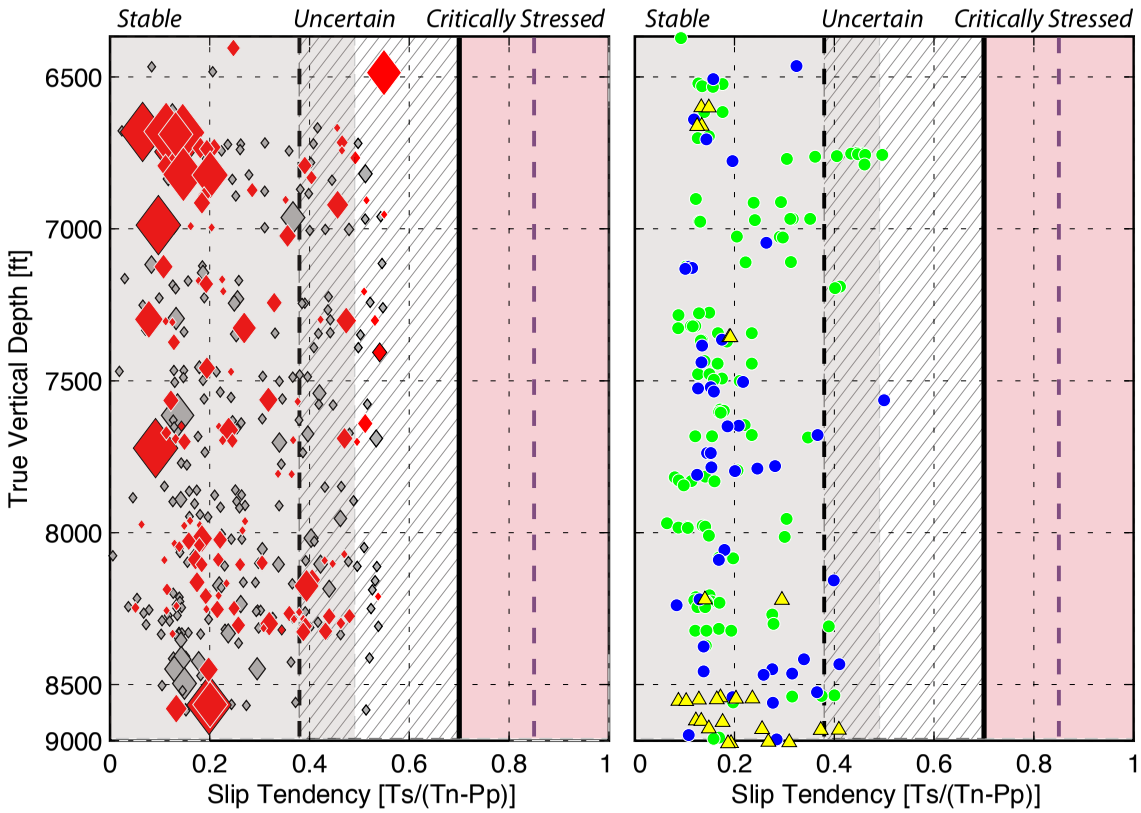
Stable
Uncertain
Critically Stressed
Stable
Uncertain
Critically Stressed
True Vertical Depth [ft]
6500
7000
7500
8000
8500
9000
0
0.2
0.4
0.6
0.8
1
Slip Tendency [Ts/(Tn-Pp)]
0
0.2
0.4
0.6
0.8
1
Slip Tendency [Ts/(Tn-Pp)]